

Article

Solar Carbo-Thermal and Methano-Thermal Reduction of MgO and ZnO for Metallic Powder and Syngas Production by Green Extractive Metallurgy

Srirat Chuayboon ¹  and Stéphane Abanades ^{2,*} 

¹ Department of Mechanical Engineering, King Mongkut's Institute of Technology Ladkrabang, Prince of Chumphon Campus, Chumphon 86160, Thailand; srirat.ch@kmitl.ac.th

² Processes, Materials and Solar Energy Laboratory, PROMES-CNRS, 7 Rue du Four Solaire, 66120 Font-Romeu, France

* Correspondence: stephane.abanades@promes.cnrs.fr; Tel.: +33-(0)4-6830-7730

Abstract: The solar carbo-thermal and methano-thermal reduction of both MgO and ZnO were performed in a flexible solar reactor operated at low pressure through both batch and continuous operations. The pyro-metallurgical process is an attractive sustainable pathway to convert and store concentrated solar energy into high-value metal commodities and fuels. Substituting fossil fuel combustion with solar energy when providing high-temperature process heat is a relevant option for green extractive metallurgy. In this study, a thermodynamic equilibrium analysis was first performed to compare the thermochemical reduction of MgO and ZnO with solid carbon or gaseous methane, and to determine the product distribution as a function of the operating conditions. The carbo-thermal and methano-thermal reduction of the MgO and ZnO volatile oxides was then experimentally assessed and compared using a directly irradiated cavity-type solar reactor under different operating conditions, varying the type of carbon-based reducing agent (either solid carbon or methane), temperature (in the range 765–1167 °C for ZnO and 991–1550 °C for MgO), total pressure (including both reduced 0.10–0.15 bar and atmospheric ~0.90 bar pressures), and processing mode (batch and continuous operations). The carbo-thermal and methano-thermal reduction reactions yielded gaseous metal species (Mg and Zn) which were recovered at the reactor outlet as fine and reactive metal powders. Reducing the total pressure favored the conversion of both MgO and ZnO and increased the yields of Mg and Zn. However, a decrease in the total pressure also promoted CO₂ production because of a shortened gas residence time, especially in the case of ZnO reduction, whereas CO₂ formation was negligible in the case of MgO reduction, whatever the conditions. Continuous reactant co-feeding (corresponding to the mixture of metal oxide and carbon or methane) was also performed during the solar reactor operation, revealing an increase in both gas production yields and reaction extent while increasing the reactant feeding rate. The type of carbon reducer influenced the reaction extent, since a higher conversion of both MgO and ZnO was reached when using carbon with a highly available specific surface area for the reactions. The continuous solar process yielded high-purity magnesium and zinc content in the solar-produced metallic powders, thus confirming the reliability, flexibility, and robustness of the solar reactor and demonstrating a promising solar metallurgical process for the clean conversion of both metal oxides and concentrated solar light to value-added chemicals.

Keywords: thermochemical conversion; concentrated sunlight; solar reactor; solar fuel; metallurgy; carbo-thermal reduction; zinc; magnesium; continuous processing



Citation: Chuayboon, S.; Abanades, S. Solar Carbo-Thermal and Methano-Thermal Reduction of MgO and ZnO for Metallic Powder and Syngas Production by Green Extractive Metallurgy. *Processes* **2022**, *10*, 154. <https://doi.org/10.3390/pr10010154>

Academic Editor: Andrey Voshkin

Received: 22 November 2021

Accepted: 10 January 2022

Published: 13 January 2022

Publisher's Note: MDPI stays neutral with regard to jurisdictional claims in published maps and institutional affiliations.



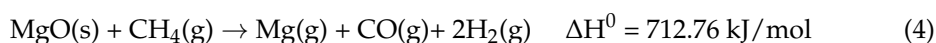
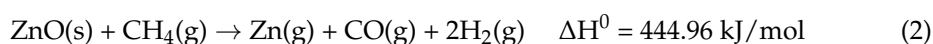
Copyright: © 2022 by the authors. Licensee MDPI, Basel, Switzerland. This article is an open access article distributed under the terms and conditions of the Creative Commons Attribution (CC BY) license (<https://creativecommons.org/licenses/by/4.0/>).

1. Introduction

Due to the major concerns related to the diminution of fossil fuels reserves, climate change, and global warming, renewable energy sources have been increasingly used to replace fossil fuels. The leading renewable energy sources consist of solar, biomass,

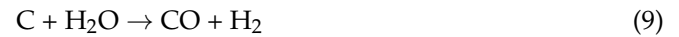
hydropower, wind, and geothermal. Solar energy is the most abundant renewable energy resource available on Earth. Every hour, the Sun delivers enough energy to the Earth to meet global energy consumption demands for an entire year, demonstrating the large solar energy potential [1]. However, the direct utilization of solar energy is limited because of its intermittency and dilution [2], and concentration after collection and subsequent storage are needed. Solar thermochemical conversion processes involve different approaches, such as gasification [3–6], carbothermal reduction [7], direct or chemical looping methane reforming [8] (including also methano-thermal reduction [9]), and two-step steam/CO₂ splitting [10]. They all represent an attractive avenue for converting intermittent and dilute sunlight into liquid/gaseous fuels and chemical commodities. Among them, the solar metallurgical carbo-thermal reduction (CTR) and methano-thermal reduction (MTR) of metal oxides (MOs) represents a promising route for producing metals and carbon monoxide (CO) or syngas (H₂ + CO) in a single reaction [9,11]. Substituting fossil fuel combustion with solar energy for providing high-temperature process heat is a relevant option for green extractive metallurgy.

MOs can be classified into two groups depending on the presence or absence of phase change during their reaction. Non-volatile MOs, such as iron oxides (Fe₂O₃/Fe₃O₄, ferrites [12]), perovskites (e.g., La_{1-x}Sr_xMnO_{3-δ}) [13,14], and ceria (CeO_{2-δ}) [11,15–17], deal with solid state reactions over the entire process. Thus, only oxygen is released from their structures, bypassing the recombination issue experienced during gas cooling at the reactor outlet. Generally, non-volatile MOs are used as oxygen carriers in H₂O/CO₂ splitting redox cycle systems [18] and chemical-looping reforming [19]. However, their drawbacks are related to their physicochemical characteristics, such as sintering (iron oxides) [12] and non-stoichiometric reactions (in the case of ceria and perovskites) [20]. Volatile MOs involve a solid-to-gas/liquid phase transition of the products (either gaseous: ZnO/Zn [21,22] and MgO/Mg [23], or liquid: SnO₂/Sn [24–26]) in the reduction step. The reduced product species first vaporize and, when the temperature decreases, they condense in the form of fine droplets or solid particles. In contrast to the non-volatile MOs, volatile MOs exhibit high oxygen exchange capacity, as they can be completely reduced to their metallic elements [27]. However, volatile MOs display a recombination issue with O₂, which can be alleviated by gas quenching [25]. In contrast to the thermal reduction of metal oxides exhibiting recombination issues with released oxygen, the utilization of carbon-based reducing agents (either solid carbon or methane) generates both carbon monoxide (or syngas) and metals in a gaseous phase with alleviated recombination issues, resulting in high metal production yields and metal oxide conversion. In this work, two attractive volatile MO candidates (ZnO and MgO) are selected to experimentally study the solar CTR and MTR of ZnO and MgO into Zn and Mg (with CO or syngas as co-products). The overall stoichiometric CTR and MTR reactions of ZnO and MgO are represented according to Equations (1)–(4):



For the CTR reactions in Equations (1) and (3), solid carbon (C) is utilized as a reducing agent to both extract oxygen from MOs and lower the thermodynamic barrier, as compared to the thermal-only dissociation of metal oxides [28], thereby producing both metals and CO [29]. For the MTR reactions in Equations (2) and (4), gaseous methane (CH₄) is used as a reducing agent. Thus, such reactions involve both the partial oxidation of CH₄ to form syngas and the simultaneous MO reduction, thereby yielding both metals and syngas [30].

Possible secondary side reactions may occur during ZnO or MgO reduction with solid carbon or gaseous methane [31] according to Equations (5)–(10):



In particular, ZnO reduction with CO or H₂ is possible, yielding Zn with CO₂ (Equation (11)) or H₂O (Equation (12)), respectively. Note that MgO reduction with CO or H₂ is not favorable according to thermodynamic analysis [29].



Hence, the overall side reaction of ZnO with methane yielding Zn, CO₂, and H₂O can be represented according to Equation (13):



MgO or ZnO conversion (X_{MgO} or X_{ZnO}) is defined as the net fraction of MgO or ZnO converted to Mg or Zn (also corresponding to Mg or Zn yield), and is obtained from an oxygen balance according to Equation (14) for the CTR of ZnO and MgO and Equation (15) for the MTR of ZnO and MgO [32]:

$$X_{\text{MO}} = \frac{n_{\text{CO}} + 2n_{\text{CO}_2}}{n_{\text{MgO}}(n_{\text{ZnO}})} \quad (14)$$

$$X_{\text{MO}} = \frac{n_{\text{CO}} + 2n_{\text{CO}_2} + n_{\text{H}_2\text{O}}}{n_{\text{ZnO}}} \quad (15)$$

where n_{CO} and n_{CO_2} indicate the total mole amounts of produced CO and CO₂ obtained by the time integration of their production rates over the reaction duration.

The solar-to-fuel energy conversion efficiency ($\eta_{\text{solar-to-fuel}}$) indicates how well solar energy is utilized as an energy source for chemical fuel production (Equation (16)):

$$\eta_{\text{solar-to-fuel}} = \frac{(LHV_{\text{syngas}} \cdot m_{\text{syngas}}) + (m_{\text{metal}}\Delta H_{\text{metal}} + 0.5O_2 \rightarrow \text{metal oxide})}{\dot{Q}_{\text{solar}} + (LHV_{\text{reductant}} \cdot m_{\text{reductant}})} \quad (16)$$

where LHV represents the lower heating value (J/kg), m is the mass flow rate (kg/s), ΔH is the standard enthalpy change (J/kg), and \dot{Q}_{solar} is the total solar power input (W) during the reaction (CO or syngas evolution period). The efficiency definition given in Equation (16) is commonly used when using carbonaceous feedstocks to account for the energy content of the feedstock (the reductant in this study is carbon or methane) in addition to the solar energy input. Additional energy requirements (e.g., for inert gas generation) are also part of the energy consumption, but the additional energy inputs (inert gas generation/recycling, gas pumping, solid feeding, synthesis of fine raw material and fine carbon, etc.) are not considered in the calculation because they depend mostly on the process and reactor scale. The nitrogen flow is arbitrary, and it is mainly linked to the use of a window (for gas sweeping) and to the need for a carrier gas for the analytical system (for gas species dilution in the measurement range). The amount of inert gas could be reduced without strongly

affecting the reactor performance; thus, it was decided to not include such parasitic energy requirements that can be lowered in a large-scale process.

Generally, the Mg product can be utilized in various applications, such as magnesium-based alloys [33], while the Zn product can be used as material for several industrial sectors, such as galvanizing and electrical batteries. Furthermore, both Mg and Zn can be used as oxygen carriers in a $\text{H}_2\text{O}/\text{CO}_2$ splitting redox cycle [34,35]. Conventionally, Mg is produced through Pidgeon, Magnetherm, and electrolytic methods [36], while Zn is extracted from ores via smelting and refining processes [37]. Such conventional approaches result in strong CO_2 emissions. As described in Equations (1)–(4), the enthalpy changes of reactions between ZnO and MgO are different. On the one hand, MgO reduction displays significantly higher ΔH^0 than ZnO reduction, implying a higher potential for solar energy storage at the expense of higher solar heat requirement. On the other hand, the lower ΔH^0 for ZnO reduction leads to a lower solar heat requirement and temperature, implying a simpler reactor process operation. Hence, the different characteristics of MOs (ZnO and MgO) and reducers (C and CH_4) motivate a comparative study of solar process performance.

In addition, ZnO or MgO reduction under low pressure is favorable for decreasing the operating temperature [7,38,39], enhancing reaction kinetics [21], and improving MO conversion. The vacuum CTR of MgO has mainly been studied theoretically [39–43]. This concept would improve the MgO reduction rate and conversion, at the expense of the pumping energy requirement [44,45]. The vacuum CTR of ZnO in a drop-tube reactor at 1–960 mbar was studied [46]. It was found that Zn production at 100 mbar was better than at ambient pressure, and at 1 mbar, the reaction was limited because of both insufficient particle residence time and inefficient heat transfer. Most of the previous research has studied ZnO or MgO reduction with solid C or CH_4 separately, and has mainly focused on thermodynamic analysis [40]. The experimental comparison of the CTR and MTR of ZnO and MgO has not been investigated yet.

Therefore, the present work aims to further explore the thermodynamics and to carry out an experimental study for the comparison of the solar CTR and MTR of ZnO and MgO in a metallurgical vacuum solar reactor. Thermodynamic analysis was first performed to identify the theoretically possible chemical reactions and equilibrium species distribution. Then, on-sun experiments of the CTR and MTR of ZnO and MgO were conducted in batch and in continuous processing modes under both reduced and atmospheric pressures. The results in terms of syngas production rate, syngas yield, and MO conversion for the CTR and MTR of ZnO and MgO were analyzed and compared. The flexibility, reliability, and robustness of this metallurgical process for the co-production of metals (Zn or Mg) and product gases (CO or syngas) were demonstrated.

2. Materials and Methods

MgO and ZnO (particle size: 1–2 μm , 99.8% purity) powders were obtained from Alfa Aesar. Two solid carbon sources, including activated charcoal (AC, 99.9% purity, <149 μm average primary particle size, and 732 m^2/g specific surface area) and carbon black (CB, 99.999% purity, 15.10⁻³ μm average primary particle size, and 210 m^2/g specific surface area), were utilized. AC was purchased from Sigma Aldrich while CB was supplied by Asahi Carbon (Japan). Concerning CTR, MOs and solid carbon were mechanically mixed with C/MO molar ratios of 1.5 (50% excess of carbon) to favor MO conversion.

Figure 1 shows the schematic diagram of the continuous 1.5 kW_{th} metallurgical solar reactor driven by highly concentrated sunlight, delivered by a 2 m-diameter parabolic concentrator located above the reactor (with a 0.85 m focal distance, a solar concentration ratio up to 10,551 suns, resulting in a peak flux density of ~10.5 MW/m^2 for a direct normal irradiation (DNI) of 1 kW/m^2). Additional details of this solar reactor have been previously described [29], and the key information is reported here. The reactor was designed and fabricated for flexible and multifunctional operation. Indeed, it can be operated in both batch and continuous processing modes under vacuum and atmospheric

pressures at various reduction temperatures (ramp and isothermal temperatures, in the range up to ~ 1600 °C). The cylindrical reactor consists of an alumina reactor cavity with a 0.12-L volume that is insulated by a porous ceramic insulation layer. Calcined alumina particles were positioned on top of the alumina wool in order to help the propagation of the CH_4 reducer. Note that no side reaction involving alumina (such as reactions forming aluminum carbide or nitride) was observed at the considered experimental conditions, and the alumina remained stable. One pressure sensor is used to measure the pressure in the reactor cavity (P), and one temperature measurement (B-type thermocouple) is installed inside the cavity (T_1). A solar-blind pyrometer ($T_{\text{pyrometer}}$) located at the center of the facedown parabolic concentrator also measures the temperature inside the cavity receiver, which can be compared with T_1 .

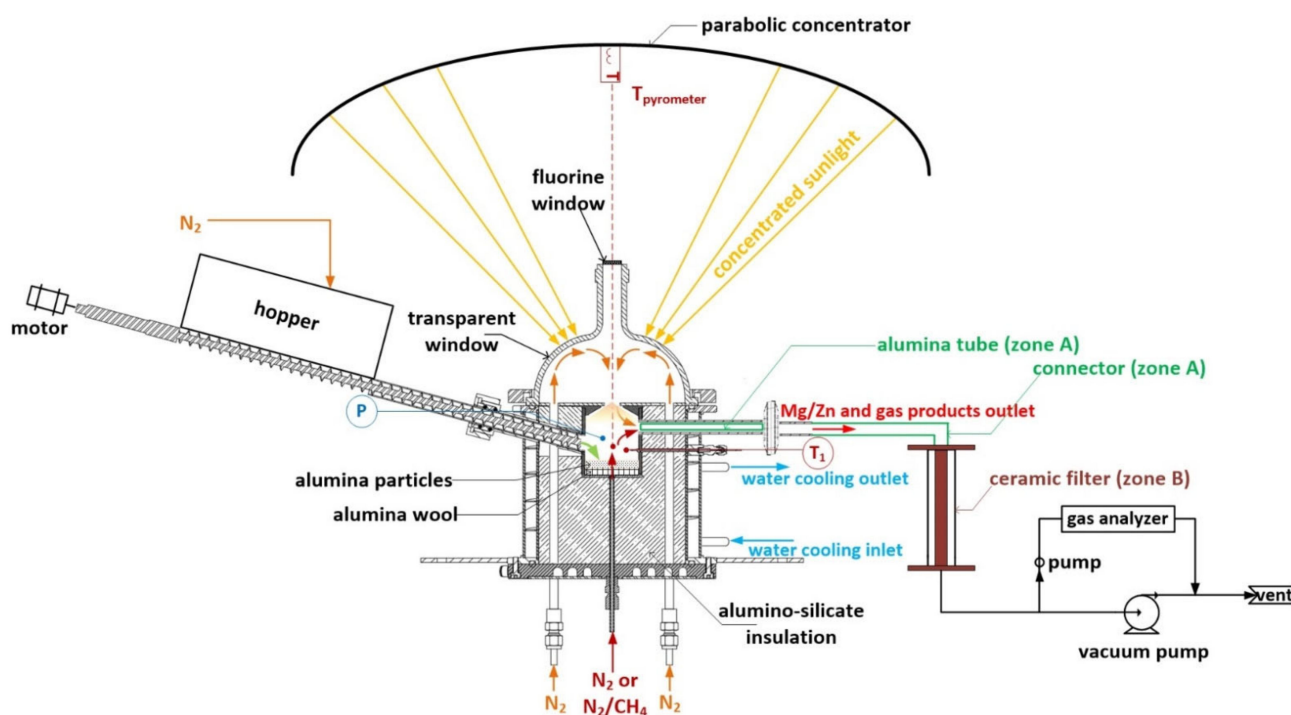


Figure 1. Schematic illustration of the 1.5 kWth metallurgical solar reactor driven by concentrated sunlight for the CTR and MTR of ZnO and MgO. Reproduced with permission from Chuayboon and Abanades [29]; *Journal of Cleaner Production*; published by Elsevier, 2019.

For the CTR of MgO and ZnO, a homogeneous mixture of metal oxide and carbon was loaded directly inside the reactor cavity receiver, and the reaction occurred during solar heating under non-isothermal conditions. For the continuous operation, a mixture of ZnO and C was placed in the hopper instead (Figure 1), and it was then fed into the heated receiver via a particle delivery system, mainly consisting of a hopper, screw feeder, and electrical motor. For the MTR of MgO and ZnO, MOs were loaded inside the cavity receiver prior to the experiments. Then, CH_4 (99.99% purity) was injected when the targeted operating temperature was stable.

The solar reactor was positioned at the focus of the vertical axis of the parabolic dish solar concentrator. Prior to each experiment, vacuum leak tests were conducted several times to ensure the absence of leaks in the reactor system. The solar reactor was heated progressively with highly concentrated sunlight to the desired temperature. During reactor heating, a N_2 protective gas flow of 2 NL/min was injected to protect the transparent window, and another N_2 flow of 0.5 NL/min was supplied to prevent the backflow of hot gases through the screw path (in the case of continuous reactant particle injection, Figure 1). Once it reached the temperature of 650 °C (for the CTR and MTR of ZnO in the batch operation) and 900 °C (for the CTR and MTR of MgO in the batch operation), the reactor

was sucked with a rotary vane vacuum pump to the targeted pressure (0.10–0.15 bar), and the reactor pressure kept stabilized, confirming that the set-up was airtight. During reactor heating, the reduction reaction occurred from ~750 °C (for the CTR of ZnO) and ~1000 °C (for the CTR of MgO), as reflected by the CO and CO₂ formation detected by an online gas analyzer. The solar heat supply rate was kept constant (~50% shutter opening for the CTR of ZnO and 100% shutter opening for the CTR of MgO). For the MTR of ZnO or MgO, once the targeted temperature was stable, the CH₄ flow (0.1 NL/min) was fed along with a carrier N₂ flow of 0.2 NL/min into the packed bed of MOs (MgO or ZnO) under isothermal operations. The solar heat input was adjusted by an automatic shutter to maintain isothermal operations.

A small portion of product gases were sucked by a secondary membrane pump to the online syngas analyzer for the continuous analysis of the product gas species (CO, H₂, CH₄, and CO₂). The syngas yields (in the unit of mmol per gram MOs, mmol/(g_{ZnO} or g_{MgO})) were calculated according to the time integration of the gas species production rates over the experiment duration. Finally, the condensed solid products that were deposited in the removable outlet reactor components (divided into two zones: zone A and zone B) were collected and subsequently analyzed via calibrated X-ray diffraction (XRD) for phase identification. Particle morphology analysis was carried out using a field emission scanning electron microscope (FESEM).

3. Results and Discussion

3.1. Thermodynamic Equilibrium Analysis

Figure 2 represents the variation of the Gibbs free enthalpy as a function of the temperature for both the MgO and ZnO reduction reactions. The most favorable reactions are the reduction of MgO and ZnO with CH₄ and solid C ($\Delta G^\circ < 0$). MgO can theoretically be reduced above ~1490 °C with CH₄ and ~1846 °C with C (at 1 bar), while ZnO can theoretically be reduced above ~840 °C with CH₄ and ~948 °C with C (at 1 bar). In contrast, the reduction reactions with H₂ and CO are favorable at much higher temperatures than with CH₄ and C. Regarding the thermal reduction ($\text{MO} \rightarrow \text{M}(\text{g}) + \frac{1}{2}\text{O}_2$), the reactions are only possible above 3433 °C for MgO and 2068 °C for ZnO (at 1 bar). Consequently, the MTR and CTR of MgO and ZnO (Equations (1)–(4)) are the most thermodynamically favorable routes for the production of Mg and Zn using solar thermochemistry.

Thermodynamic equilibrium calculations based on the principle of the Gibbs free enthalpy minimization were carried out using HSC Chemistry software to predict the products' distribution for both the MTR and CTR of MgO and ZnO. The approach assumes a closed system (no species inlet and outlet) and does not take into account any kinetic aspect. This approach was used to predict the theoretical limit of the reduction reactions and to identify the expected products as a function of the main operating parameters.

The operating pressure is a key factor influencing the equilibrium of the reduction reactions of MgO and ZnO for both MTR and CTR. As the reaction produces gas species (both gaseous metal and CO or syngas), decreasing the total pressure favors the shift of the equilibrium of the reduction reactions towards product formation according to Le Chatelier's principle. This is confirmed by Figures 3 and 4, which show the effect of the total pressure on the products' equilibrium distribution for both the CTR and MTR of MgO and ZnO. Regarding CTR (Figure 3), the reaction is complete below 0.4 bar at 1500 °C for MgO (Mg(g) and CO are the only species at equilibrium), whereas it is complete below 0.4 bar at 750 °C for ZnO. Above this pressure, the products are still formed, but their amounts decrease with increasing pressure. Regarding MTR (Figure 4), similar conclusions can be formulated, since the methane is first dissociated to solid C and H₂, as indicated by the amount of H₂ being constant and equal to 2 mol, while the produced C reacts with MgO or ZnO in the same way as CTR.

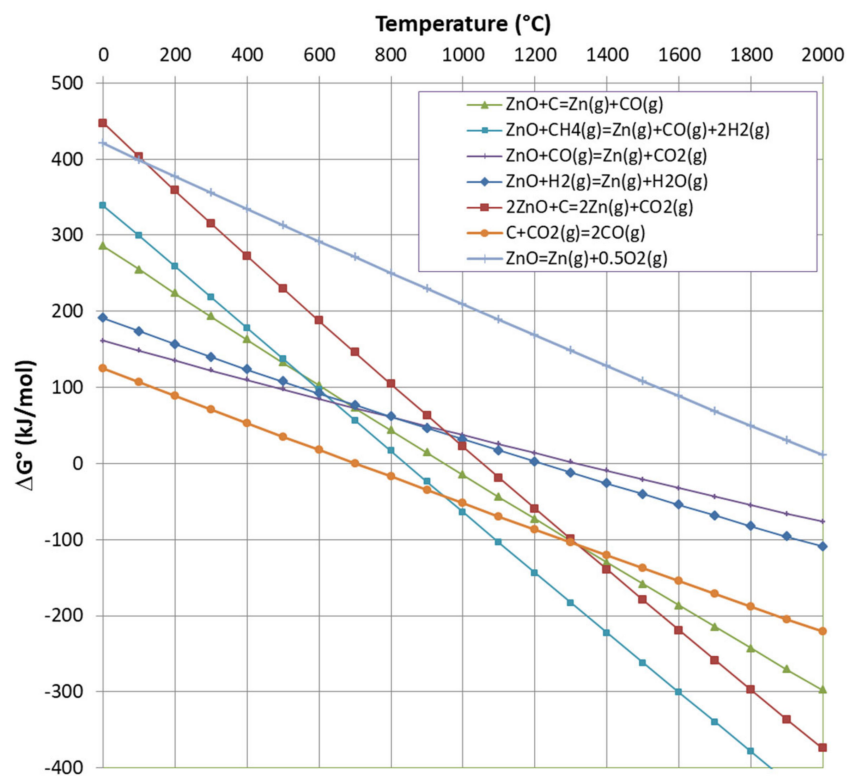
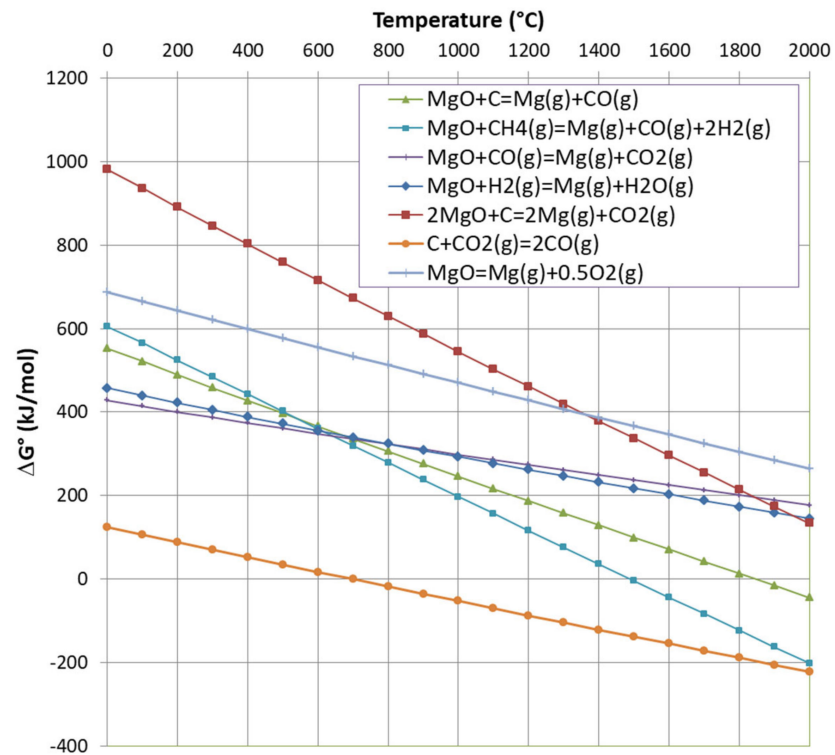
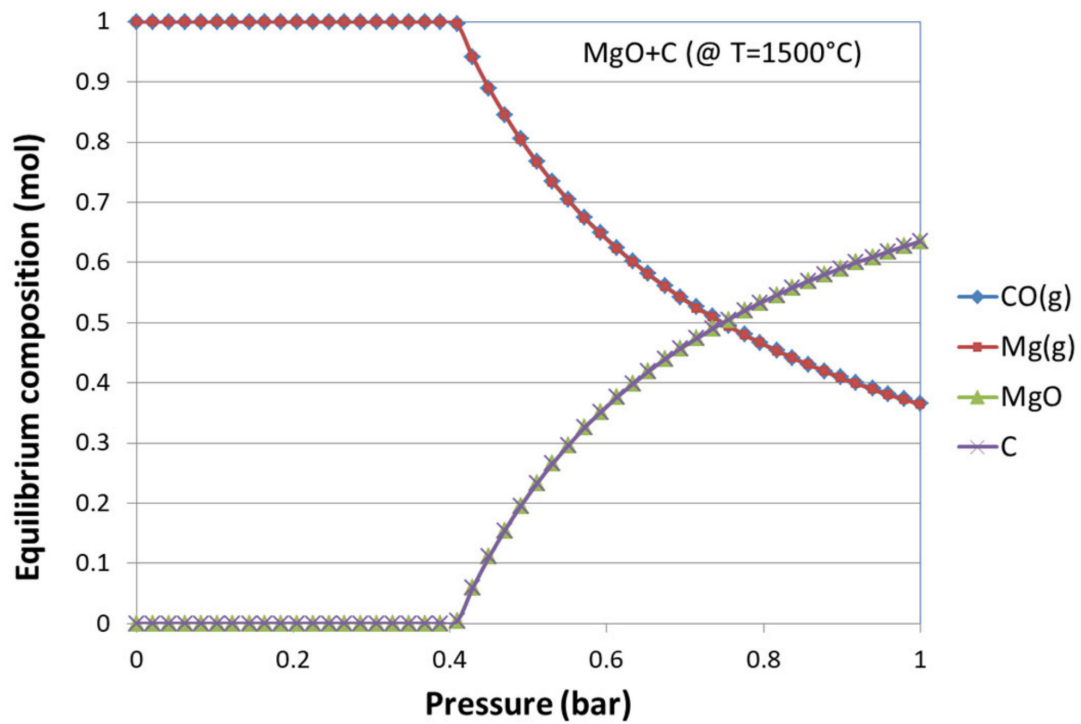
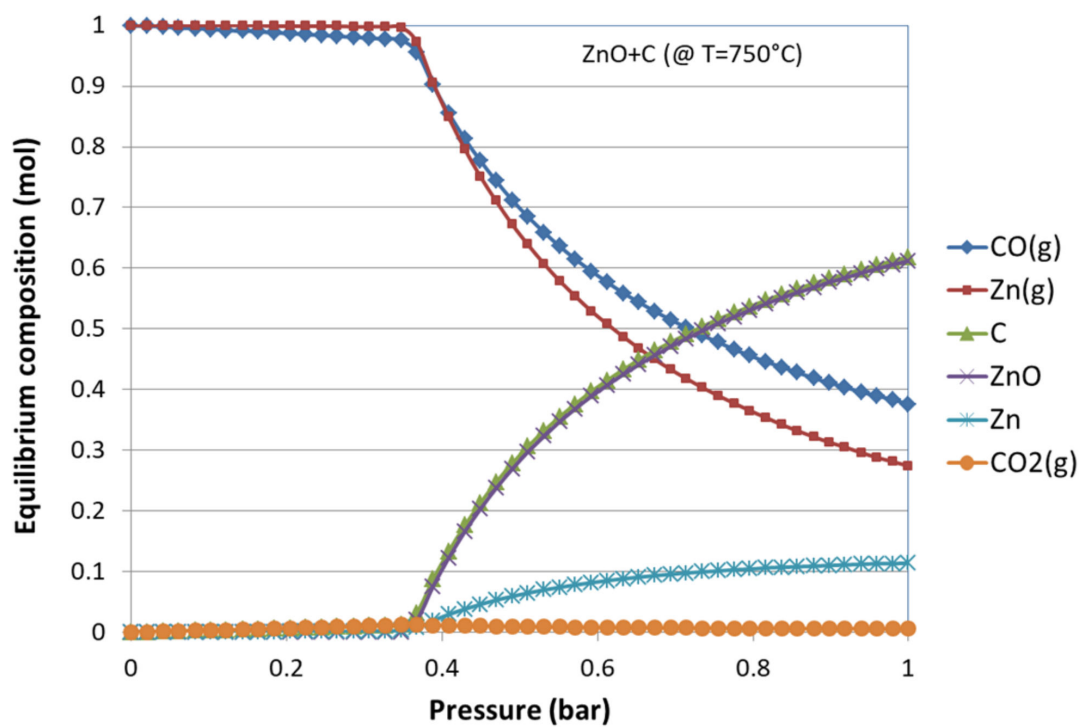


Figure 2. Evolution of Gibbs free enthalpy versus temperature of the main reduction reactions involving (a) MgO and (b) ZnO.

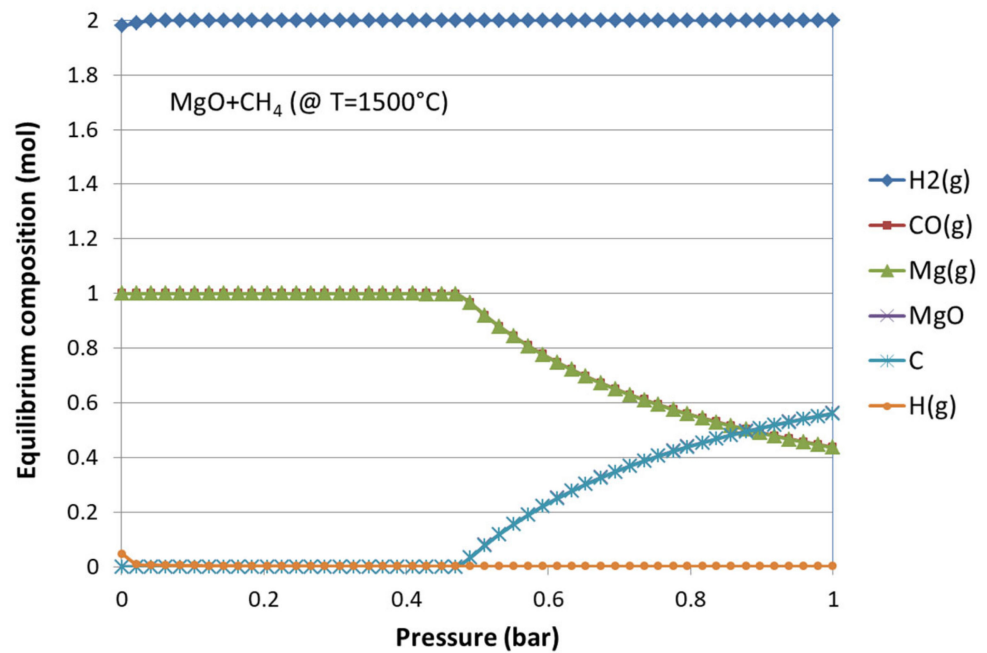


(a)

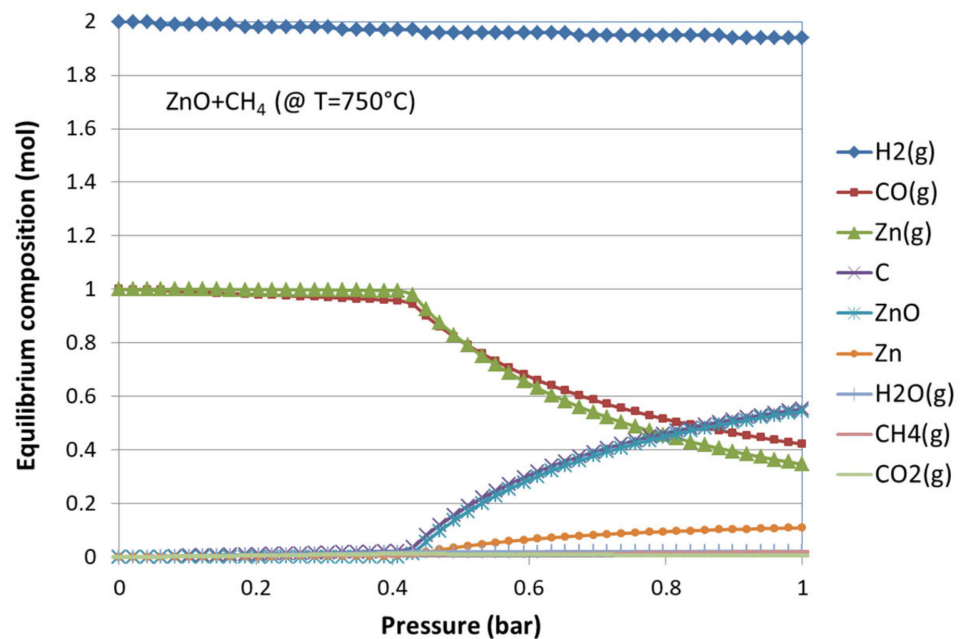


(b)

Figure 3. Influence of total pressure on equilibrium product distribution for the carbo-thermal reduction of (a) MgO (at 1500°C) and (b) ZnO (at 750°C).



(a)



(b)

Figure 4. Influence of total pressure on equilibrium product distribution for the methano-thermal reduction of (a) MgO (at 1500 °C) and (b) ZnO (at 750 °C).

The effect of temperature was also investigated at thermodynamic equilibrium for both the MTR and CTR of MgO and ZnO. The CTR is theoretically complete above 1600 °C for MgO and 800 °C for ZnO (at 1 bar), with the gaseous metal and CO being the only products at equilibrium (Figure 5). The formation of CO₂ remains negligible whatever the temperature according to the thermodynamics. Regarding MTR (Figure 6), similar conclusions can be stated, although CH₄ is first decomposed to H₂ and C, and the latter can react with the oxide in the same way as with CTR.

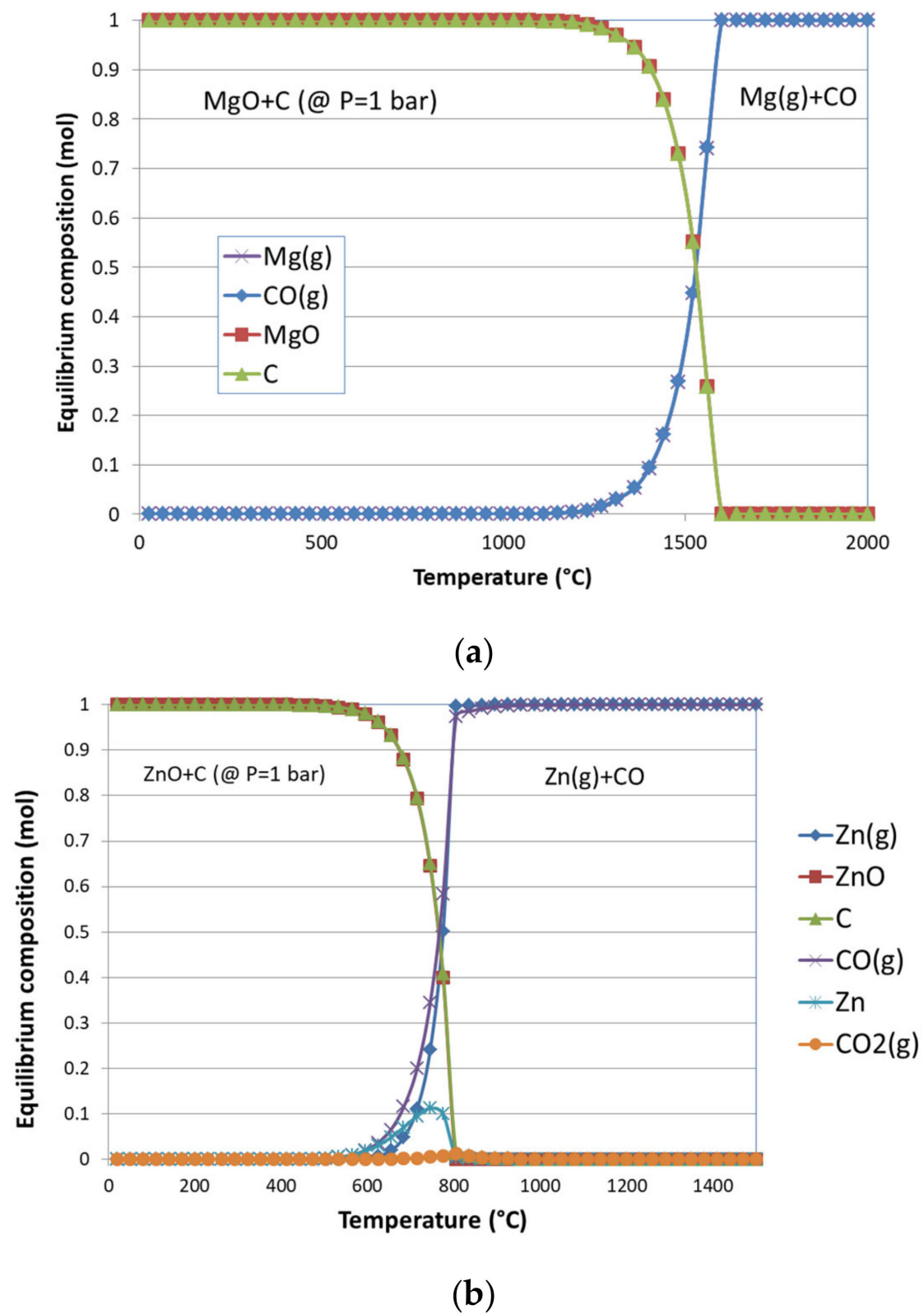


Figure 5. Influence of temperature on equilibrium product distribution for the carbo-thermal reduction of (a) MgO and (b) ZnO (at $P = 1$ bar).

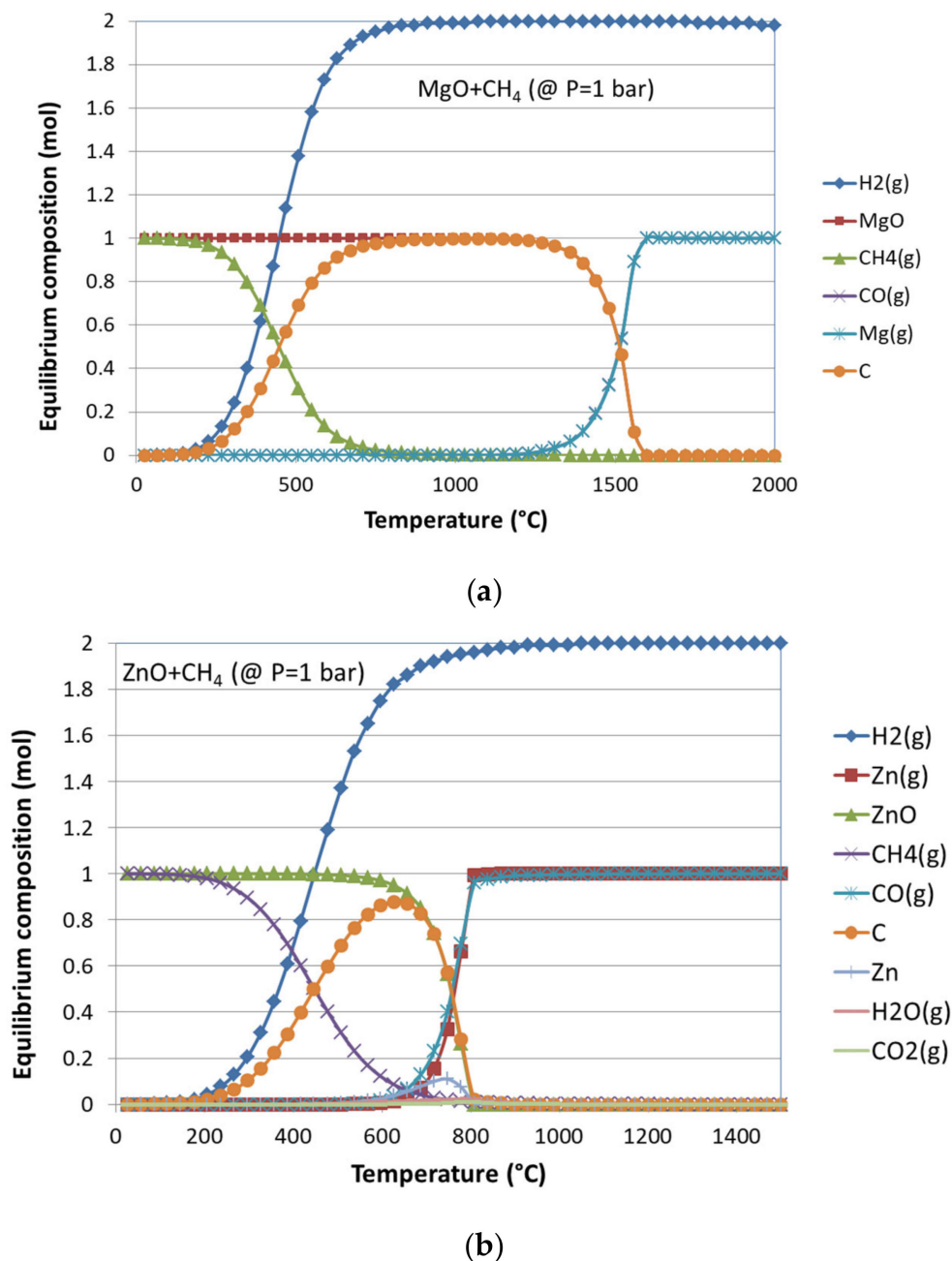


Figure 6. Influence of temperature on equilibrium product distribution for the methano-thermal reduction of (a) MgO and (b) ZnO (at $P = 1$ bar).

The thermodynamic predictions provide the theoretical limits of the reduction reactions for a closed system. In a real reactor with species transport between the inlet and outlet, fresh reactants are continually supplied and the products can be continually removed from the reaction site, which favors the thermodynamic equilibrium shift towards product formation. The continuous removal of products indeed shifts the reactions to the product side and favors reaction completion. Thus, the temperature and pressure conditions can be optimized in comparison with the thermodynamic limits. In practice, the reduction reactions with either carbon or methane can thus be carried out at lower temperatures or higher pressures than the values determined at the thermodynamic equilibrium. An experimental study was then performed to investigate the reduction reactions of both

MgO and ZnO in a solar reactor operated in batch or in continuous processing modes to determine the suitable conditions for Mg and Zn metallic powder production.

3.2. Solar Reactor Performance Evaluation

Table 1 lists the operating conditions and experimental results of the CTR and MTR of MgO and ZnO in batch and in continuous operation under vacuum and atmospheric pressures. On-sun experiments were carried out under the following range of parameters: $P = 0.10\text{--}0.90$ bar, $\dot{m}_N = 2.2\text{--}2.7$ NL/min, $\dot{Q}_{solar} = 0.73\text{--}1.32$ kWth, with reducing agents consisting of solid carbon (AC and CB) with a (AC or CB)/(MgO or ZnO) molar ratio = 1.5 and gaseous CH_4 with a constant flow rate of 0.1 NL/min. The maximum temperatures were in the range $950\text{--}1550$ °C (T_1).

Overall, MgO conversion (X_{MgO}) was almost complete (97.8%) for the CTR of MgO, and 28.9% for the MTR of MgO. ZnO conversion (X_{ZnO}) was as high as 76.5% for the CTR of ZnO and 60.6% for the MTR of ZnO in batch mode. ZnO conversion (X_{ZnO}) in continuous CTR was in the range 44.3–47.1%. Methane conversion (X_{CH_4}) was found to be 91.7% for the MTR of MgO because of the favored CH_4 cracking reaction, and 26.6% for the MTR of ZnO.

The solar-to-fuel energy conversion efficiency ($\eta_{solar-to-fuel}$) in the range of 1.1–3.0% was achieved for the batch operation, while it was found to be superior for the continuous operation (3.2–3.3%). This can be explained by the fact that the batch operation exhibited less favorable conversion conditions due to a long non-isothermal operation period. The process efficiency can be enhanced by an isothermal continuous operation, as evidenced by a higher $\eta_{solar-to-fuel}$.

In addition, the main limitation when dealing with small-scale experiments is related to the limited solar-to-fuel efficiency due to the unfavorable heat losses. Such heat losses (especially conductive heat losses) can be lowered by reactor up-scaling (due to a reduced surface to volume ratio). In addition, inert gas requirements should be reduced at larger scales due to the cost of inert gas generation or recycling. Another technical challenge is related to the solid product recovery at the reactor outlet because of particle deposition in the outlet components on the cold surface before reaching the filter. The reduction of the area of any cold surface in large-scale reactors should alleviate this issue. Regarding Mg production, the recovery/collection of pure Mg deposited in the reactor outlet components is challenging because dispersed metallic powder tends to react upon exposure to ambient air, and metal recovery under inert atmosphere should be preferred.

3.3. Batch Carbo-Thermal/Methano-Thermal Reduction of ZnO and MgO

3.3.1. Syngas Production Rate

The on-sun CTR and MTR of ZnO and MgO were first carried out under non-isothermal and isothermal batch operation. The operating pressure was reduced to around 0.10–0.15 bar to favor MO conversion according to the above thermodynamic study. ZnO (2–2.4 g) and MgO (2 g) were reacted with solid carbon (AC) and a gaseous reducer (CH_4). The transient syngas production rates (CO , CO_2 , H_2 , and CH_4) along with reactor temperatures (T_1 and $T_{pyrometer}$) are plotted as a function of time for the CTR of MgO (Figure 7a), the MTR of MgO (Figure 7b), the CTR of ZnO (Figure 7c), and the MTR of ZnO (Figure 7d [30]). The operating temperatures (referred to as T_1) were in the range of 991–1550 °C for the CTR of MgO and 765–1167 °C for the CTR of ZnO, while those for the MTR of MgO and ZnO were controlled isothermally at 1300 °C and 1000 °C, respectively. Note that MgO reduction required a significantly higher temperature than ZnO reduction, as previously pointed out in the thermodynamic analysis.

Table 1. Operating conditions and solar reactor performance evaluation.

Run No.	Reaction	Mode	Metal Oxide Mass (g)	Reducer Flow Rate	Pressure (bar)	T _{1 max} (°C)	\dot{Q}_{solar} (kW)	CO (mmol/g _{metal oxide})	CO ₂ (mmol/g _{metal oxide})	H ₂ (mmol/g _{metal oxide})	X _{MgO} or X _{ZnO} (%)	X _{CH4} (%)	solar-to-fuel (%)
1	MgO + 1.5AC	Batch	2.0	-	0.10	1550	1.32	23.8	0.2	-	97.8	-	1.7
2	MgO + CH ₄	Batch	2.0	0.1 NL/min	0.10	1314	1.10	7.1	0.1	57.3	28.9	91.7	3.0
3	ZnO + 1.5AC	Batch	2.4	-	0.15	1167	0.82	4.2	2.6	-	76.5	-	1.1
4	ZnO + CH ₄	Batch	2.0	0.1 NL/min	0.15	1000	0.77	0.9	1.6	3.3	60.6	26.6	2.6
5	ZnO + 1.5CB	Continuous	10	0.5 g/min	0.90	950	0.80	2.1	1.7	-	44.3	-	3.3
6	ZnO + 1.5CB	Continuous	10	1.0 g/min	0.90	950	0.73	2.3	1.8	-	47.1	-	3.2

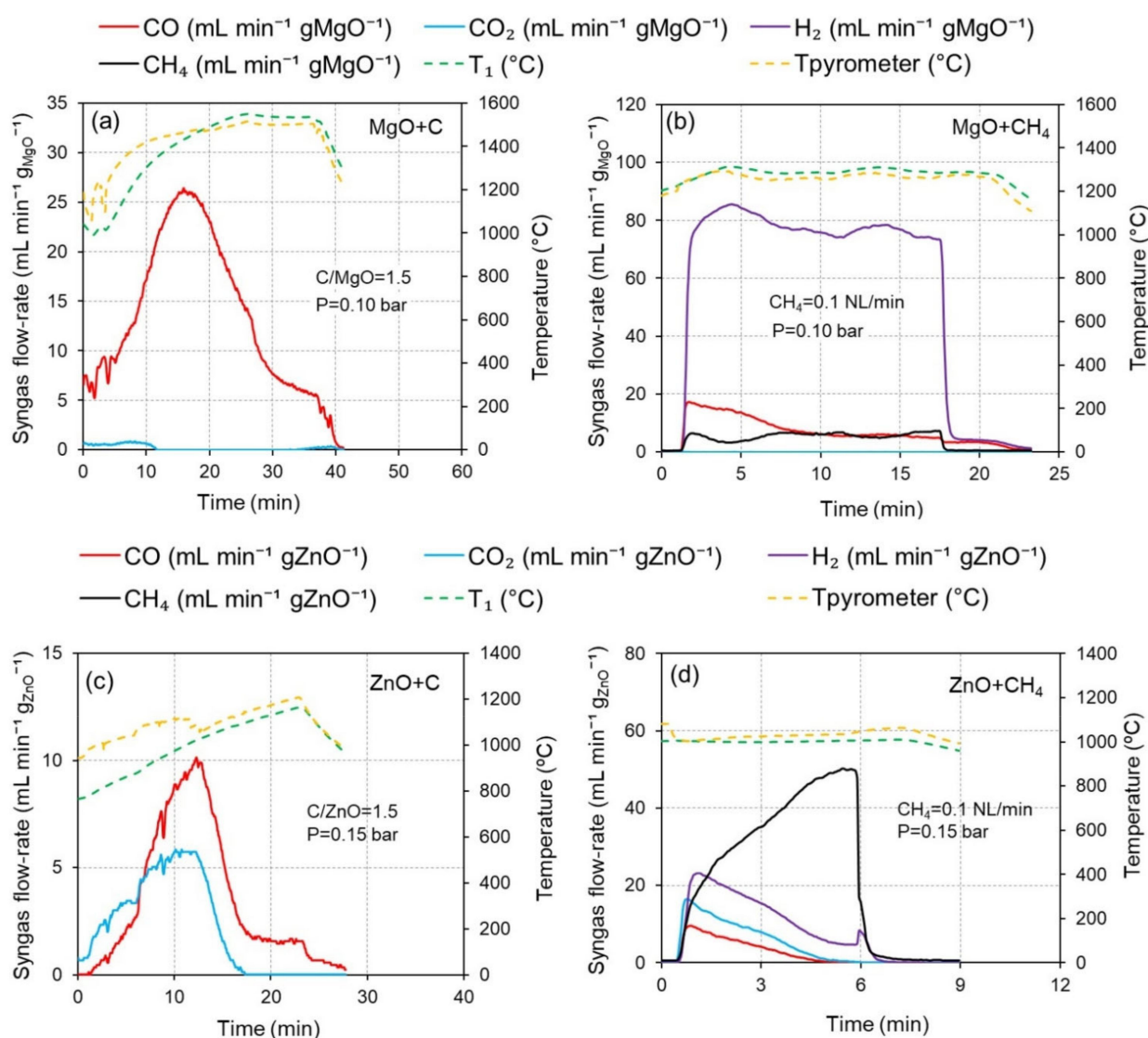


Figure 7. Syngas production rate along with reactor temperatures for the (a) CTR of MgO, (b) MTR of MgO, (c) CTR of ZnO, and (d) MTR of ZnO, under low pressure operations (0.10–0.15 bar).

Overall, a significant difference in the syngas production rate for each reaction was demonstrated. Concerning MgO reduction, the CO production rate increased with the temperature, and it appeared to be the main gas product for the CTR of MgO (Figure 7a), in agreement with the thermodynamic analysis. In contrast, the CO₂ production rate was found at the initial state only and appeared to be negligible. Regarding the MgO reaction with CH₄ (Figure 7b), the H₂ production rate became the main gas product because of a strong methane cracking reaction at 1300 °C, while the CO production rate was quite low due to a low reaction of the MTR of MgO at this temperature, in agreement with thermodynamic analysis. Similar to the CTR of MgO, no CO₂ production rate from the MTR of MgO was observed.

Concerning ZnO, the CTR (Figure 7c) and MTR (Figure 7d) of ZnO exhibited both high CO and CO₂ production rates, which differs from the MgO reduction. In contrast to the CTR of ZnO, the CO₂ production rate from the MTR of ZnO was found to be higher than the CO production rate (Figure 7d). Compared to the MTR of MgO, the H₂ production rate from the MTR of ZnO, ascribed to methane cracking, was significantly lower thanks to the considerably lower operating temperature.

3.3.2. Gas Species Production Yield

The syngas yields and metal oxide conversions are plotted for the CTR of MgO compared with the MTR of MgO (Figure 8a) and for the CTR of ZnO compared with the MTR of ZnO (Figure 8b). Differences in syngas yields and MO conversion in each reaction were obvious. Concerning MgO reduction (Figure 8a), using C as reducer resulted in a CO yield of 23.8 mmol/g_{MgO}, a CO₂ yield of 0.2 mmol/g_{MgO}, and an X_{MgO} of 97.8%, while using CH₄ as reducer resulted in a CO yield of 7.1 mmol/g_{MgO}, a CO₂ yield of 0.1 mmol/g_{MgO}, and an X_{MgO} of 28.9%. Therefore, the CTR of MgO was found to exhibit a higher X_{MgO} due to a higher temperature, while the MTR of MgO can alternatively co-produce syngas and Mg, but with high coke formation (ascribed to the methane cracking reaction, as evidenced by a steep increase in H₂ up to 57.3 mmol/g_{MgO}). The negligible CO₂ formation from the MgO reduction was likely attributed to the Boudouard equilibrium (Equation (8)), because the solid–gas reaction between MgO and CO is not thermodynamically favorable within the considered temperature range, as seen in Figure 2a.

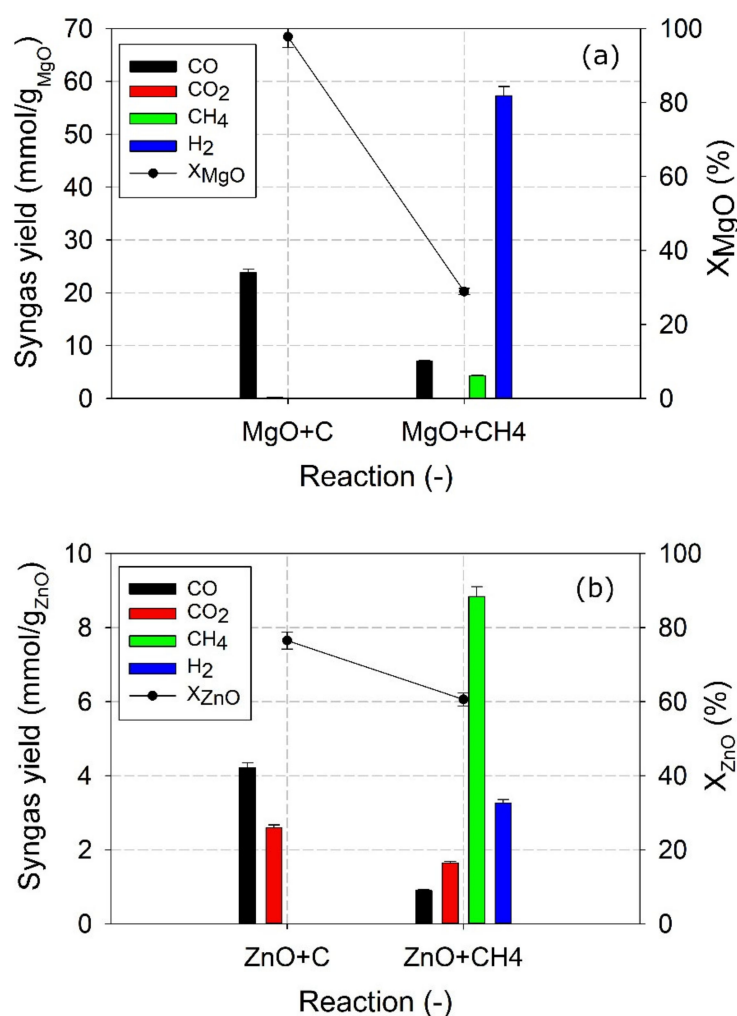


Figure 8. Syngas yields and MO conversion: (a) the CTR of MgO vs. the MTR of MgO and (b) the CTR of ZnO vs. the MTR of ZnO.

Regarding the ZnO reduction (Figure 8b), the CO and CO₂ yields were 4.2 and 2.6 mmol/g_{ZnO} for the CTR of ZnO, compared to 0.90 and 1.64 mmol/g_{ZnO} for the MTR of ZnO, respectively. The CO₂ from the MTR of ZnO appeared to be higher than CO. This is because of the effect of pressure on the different reaction mechanisms between solid–solid reactions (the CTR of ZnO) and solid–gas reactions (the MTR of ZnO). To clarify this point, the solid–gas reaction (the MTR of ZnO in Equation (2)) is more negatively influenced by

low pressure conditions than the solid–solid reaction (the CTR of ZnO in Equation (1)) because the gas residence time is decreased from reducing the pressure. This issue can also affect the side reactions in Equations (5)–(10). For these reasons, the CO₂ from the MTR of ZnO was higher than CO. X_{ZnO} was 76.5% for the CTR of ZnO, compared to 60.6% for the MTR of ZnO. X_{ZnO} of the CTR of ZnO was slightly higher in comparison to the MTR of ZnO due to the higher operating temperature.

Regarding the difference in ZnO and MgO reduction, the CO yield from the CTR of MgO (Figure 8a) was much higher than that from the CTR of ZnO. This was because the discharged oxygen from MgO is recovered mainly in the form of CO, while the discharged oxygen from ZnO is recovered in the form of both CO and CO₂. Additionally, the molecular weight of MgO is lower, given that it is around half of that of ZnO (40.30 g/mol (MgO) vs. 81.38 g/mol (ZnO)). In addition, the X_{ZnO} from the CTR was lower than the X_{MgO} from the CTR due to the possible Zn recombination with CO₂ to ZnO. The MTR of MgO occurs with stronger thermal methane decomposition than the MTR of ZnO due to the higher operating temperature. The MTR of ZnO was thus found to be more relevant than the MTR of MgO in terms of a higher MO conversion rate and a lower CH₄ cracking reaction. In summary, the difference in the thermochemical reduction behavior and the effect of pressure on syngas production rate, syngas yield, and MO conversion between the CTR and MTR of ZnO and MgO was thus evidenced and consistent with the thermodynamic study, showing several important findings, including the operational feasibility, reactor reliability, as well as pros vs. cons in each process.

3.4. Continuous Carbothermal Reduction

Continuous operation plays a significant role in solar processes. In this study, the continuous CTR of ZnO was experimentally investigated at atmospheric pressure (0.90 bar). CB was used as a reducer. Experiments were investigated by varying the reactant feeding rate (0.5 and 1.0 g/min) at a constant temperature of 950 °C. Note that the temperature of 950 °C was chosen to allow the direct insertion of the screw feeder tip into the cavity receiver. Before on-sun experiments, the screw feeder was first calibrated for the mixture of ZnO and CB to precisely control its mass feeding rate. A homogeneous mixture of reactant powder with a fixed CB/ZnO molar ratio of 1.5 (12 g in total mass) was prepared and fed into the cavity receiver (Figure 1). The reaction was carried out isothermally. Figure 9 shows the CO and CO₂ yields along with the X_{ZnO} as a function of the reactant feeding rate. It was found that both CO and CO₂ yields increased with the increasing reactant feeding rate, from 2.08 and 1.68 mmol/g_{ZnO} at 0.5 g/min to 2.25 and 1.77 mmol/g_{ZnO} at 1.0 g/min, thereby resulting in the X_{ZnO} increasing from 44.3% to 47.1%. From these results, it can be pointed out that increasing the feeding rate hastened the reactant consumption that promoted the gas yields. In addition, an excessively low feeding rate results in a low gas production rate and the inefficient utilization of the solar energy input, whereas an excessively high reactant feeding rate may cause reactant accumulation. Therefore, for a given temperature, the reactant feeding rate must match the reduction reaction rate to avoid the issue of reactant accumulation. In comparison, X_{ZnO} values obtained from continuous tests were much lower than those obtained in batch tests (44.3–47.1% for continuous tests vs. 76.5% for batch tests). This is just because the kinetics during isothermal operations at a constant temperature of 950 °C were lower (950 °C for continuous tests vs. ramping between 765–1167 °C for batch tests), and the reducing properties of CB used in the continuous tests were lower [29], thereby leading to a lower X_{ZnO} .

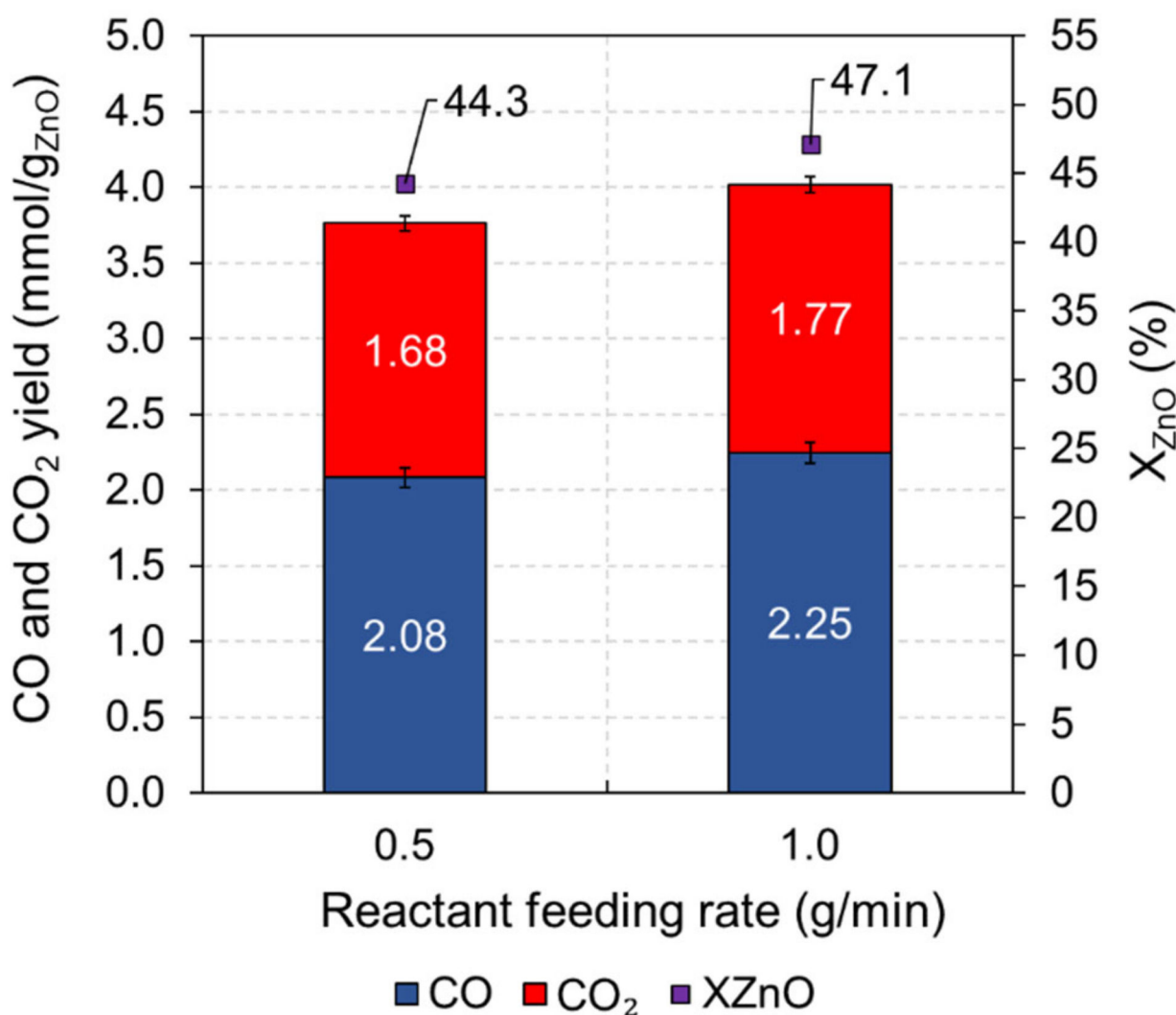


Figure 9. CO and CO₂ yields, along with ZnO conversion (X_{ZnO}) for ZnO carbothermal reduction (CB/ZnO = 1.5) during continuous powder injection.

3.5. Solid Product Characterization

Figure 10 shows the XRD patterns of the collected solid products from the CTR of MgO (Figure 10a), the MTR of MgO (Figure 10b), the CTR of ZnO (Figure 10c), and the MTR of ZnO (Figure 10d). As illustrated in Figure 1, the outlet components where the solid products were deposited were divided into two zones: (i) zone A is the collected product from the reactor outlet (both alumina tube and connector) and (ii) zone B is the collected product from the ceramic filter.

Concerning the MgO reduction, traces of MgO and Mg were identified in both zone A and zone B for the CTR of MgO (Figure 10a) and the MTR of MgO (Figure 10b), indicating partial Mg oxidation that mainly occurred during the products' collection (and/or its recombination with CO). Between zone A and zone B, Mg intensity was not significantly different. Note that, during the collection and transfer of the solid products, Mg oxidation with air was observed at ambient temperatures due to the very fine and dispersed reactive powder (composed of agglomerates of nanoparticles). This issue directly caused an increase in the MgO content in the solid products due to its contact with air (thus not caused by the reactor operation itself), which explains the presence of MgO phase in all the XRD patterns of samples from both the CTR of MgO and the MTR of MgO, whether collected from zones

A or B. Nevertheless, a very high MgO conversion of up to 97.8% (Figure 8a) can confirm almost complete MgO conversion and a high-purity Mg product.

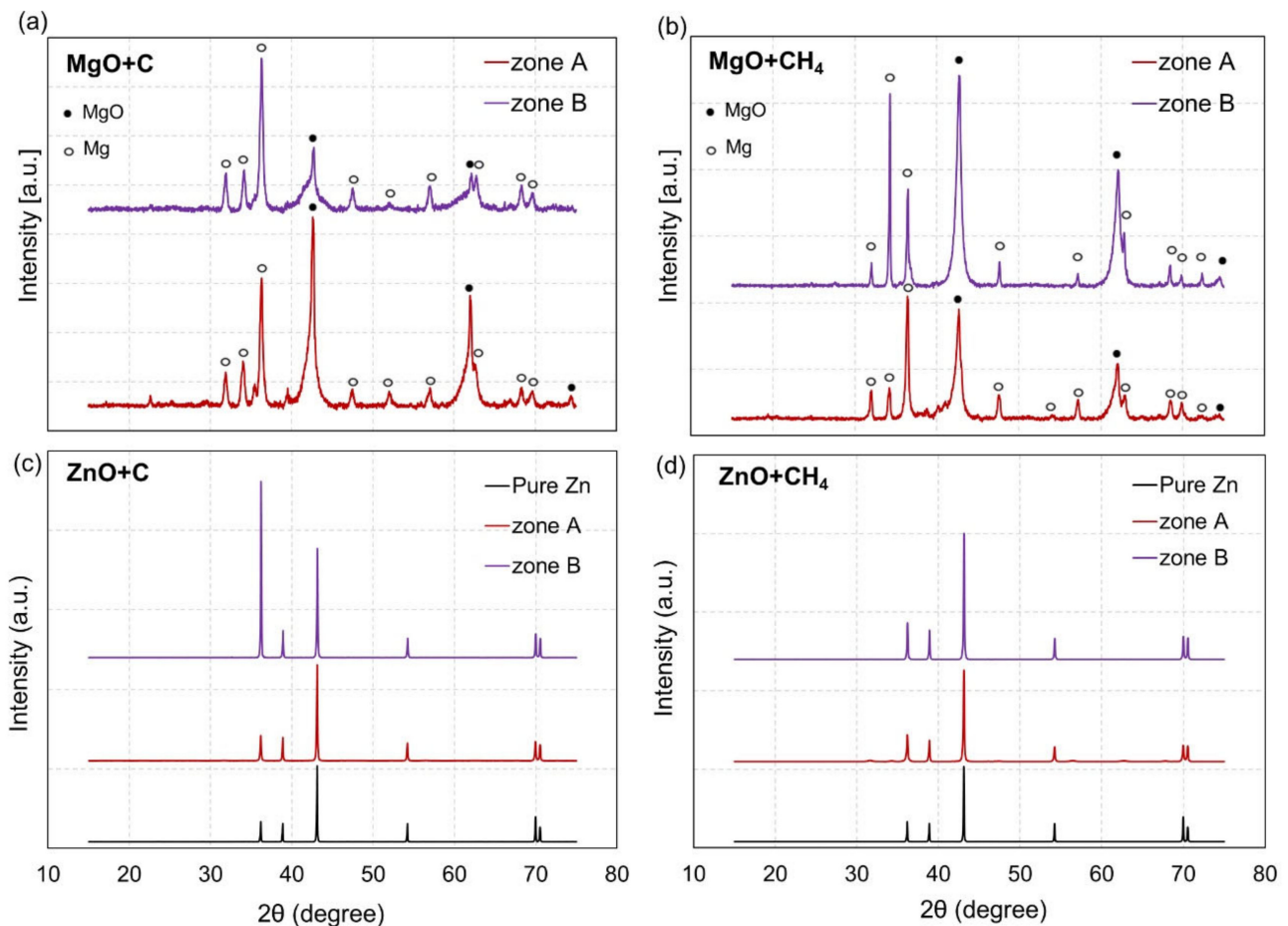


Figure 10. Representative XRD patterns of solid products from zone A and zone B: (a) the CTR of MgO, (b) the MTR of MgO, (c) the CTR of ZnO, and (d) the MTR of ZnO.

Regarding the ZnO reduction, both the CTR of ZnO (Figure 10c) and the MTR of ZnO (Figure 10d) present only the Zn pattern with a high peak intensity in both zone A and zone B, as compared with the commercially pure Zn reference pattern, thereby demonstrating high-purity Zn production in both zones and its stability in ambient air.

Figure 11 shows the particle morphology of the solid products recovered at the filter (zone B), characterized by FESEM for the CTR of MgO (Figure 11a), the MTR of MgO (Figure 11b), the CTR of ZnO (Figure 11c), and the MTR of ZnO (Figure 11d). Concerning the MgO reduction, the Mg morphology of the CTR of MgO (Figure 11a) and the MTR of MgO (Figure 11b) was similar. As seen in Figure 11b, the Mg powder is composed of fine agglomerated spherical particles, likely arising from the condensation of fine droplets. Concerning the ZnO reduction, for the CTR (Figure 11c), the Zn product grew and condensed with a hexagonal crystal structure, and some parts were enveloped by solid carbon particles. For the MTR of ZnO (Figure 11d), a clear hexagonal structure made of superposed plane layers of condensed Zn was observed, with almost no solid carbon deposition on it. A cleaner surface of the Zn product from the MTR of ZnO was achieved thanks to the use of the CH₄ reducer. In comparison, differences in the products' morphologies between the Mg and Zn particles was obvious. Mg displayed a more homogeneous distribution than Zn, and the particle size of Zn was significantly larger than Mg.

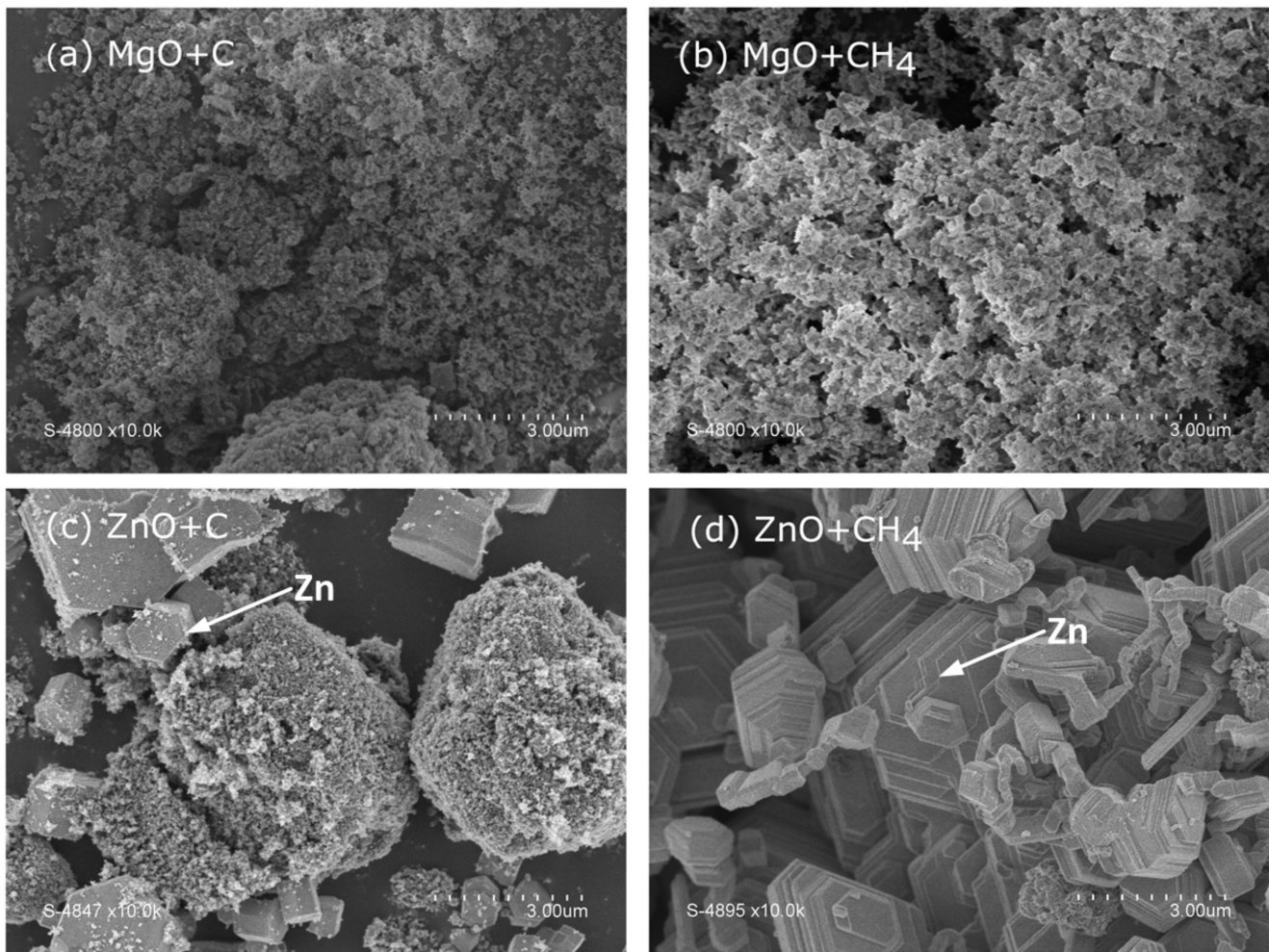


Figure 11. FESEM micrographs of solid products collected in the filter (zone B): (a) the CTR of MgO, (b) the MTR of MgO, (c) the CTR of ZnO, and (d) the MTR of ZnO.

4. Conclusions

The solar carbo-thermal reduction (CTR) and methano-thermal reduction (MTR) of ZnO and MgO was performed in a flexible solar reactor both in batch and in continuous operations under reduced (0.10–0.15 bar) and atmospheric pressures (0.90 bar), demonstrating the reliability, flexibility, and robustness of the solar-driven metallurgical process for both green metals (Zn and Mg) and sustainable syngas production in a single process. The thermodynamic analysis provided insights into the theoretically possible chemical reactions and equilibrium species distribution for comparison with experimental results. The experimental outcomes concerning syngas production rates, syngas yields, metal oxide (ZnO and MgO) conversion, as well as solar-to-fuel energy conversion efficiency, were assessed and compared with on-sun experiments. The prototype vacuum reactor was demonstrated to be flexible at processing different volatile metal oxides (MgO and ZnO) for the co-production of metallic Mg or Zn and CO or syngas in batch and in continuous modes under both low and atmospheric pressure conditions.

Solar-driven MgO and ZnO reduction with either solid carbon or gaseous methane under low pressures were compared, and proved to be feasible. A noticeable difference in the reaction mechanism between the CTR and MTR of MgO and the CTR and MTR of ZnO was demonstrated through their syngas production rate and syngas yield. Concerning MgO reduction, the CTR of MgO yielded mainly CO as high as 24.6 mmol/g_{MgO}. The MTR of MgO yielded quite a low amount of CO at the expense of a high H₂ yield due to strong thermal CH₄ decomposition at the reaction temperature. Negligible CO₂ yields

were measured from both the CTR and MTR of MgO. Almost complete MgO conversion ($X_{MgO} = 97.8\%$) was achieved from the CTR of MgO. Concerning ZnO reduction in batch operation, the CTR of ZnO yielded higher CO and CO₂ in comparison with the MTR of ZnO, but the MTR of ZnO additionally yielded H₂. However, in the MTR of ZnO, the CO₂ yield was higher than CO due to the short gas residence time caused by the reduced pressure. Regarding the continuous CTR of ZnO under isothermal conditions, an increase in the reactant feeding rate hastened ZnO consumption, which in turn promoted the ZnO conversion to 47.1% at 1 g/min. Additionally, $\eta_{solar-to-fuel}$ in the range of 1.1–3.0% was achieved for the batch operation, while it was found to be superior for the continuous operation (3.2–3.3%). Comparing the CTR of ZnO between batch and continuous operations, significantly higher reaction extents were reached in the batch tests; nevertheless, they implied a higher solar heat consumption resulting from non-isothermal operation (i.e., longer operating duration), which in turn led to a lower solar-to-fuel energy conversion efficiency.

Regarding the characterization of the Zn and Mg products from the CTR and MTR, Mg fine powder was produced, and it was highly reactive with air, thereby resulting in low Mg content after exposure to air based on ex situ solid product analysis. High-purity Zn powder synthesis was demonstrated, and Zn morphology clearly displayed hexagonal crystal structure with micrometric particle size. The continuous CTR and MTR of ZnO and MgO under low pressure conditions are suggested for further investigation to both enhance metal oxide conversion rates while producing metallic powders in continuous mode. Up-scaled solar reactors are also needed for green extractive metallurgy using renewable or bio-sourced reducers.

Author Contributions: S.C. and S.A. created the ideas and research design of this paper; S.C. performed data analysis; S.C. and S.A. acquired the data; S.C. wrote the original draft; S.A. reviewed and edited the paper. All authors have read and agreed to the published version of the manuscript.

Funding: This research received no external funding.

Institutional Review Board Statement: Not applicable.

Informed Consent Statement: Not applicable.

Data Availability Statement: The data presented in this study are available on request from the authors.

Acknowledgments: The authors would like to thank both the French Embassy in Thailand and Campus France for supporting the scholarship under the Junior Research Fellowship Program, 2021. This study was performed in a collaboration between PROMES-CNRS and King Mongkut's Institute of Technology Ladkrabang, Thailand. The material characterization platform (E Beche) is acknowledged for their support in the XRD analysis.

Conflicts of Interest: The authors declare no conflict of interest.

References

1. Chuayboon, S.; Abanades, S. An overview of solar decarbonization processes, reacting oxide materials, and thermochemical reactors for hydrogen and syngas production. *Int. J. Hydrog. Energy* **2020**, *45*, 25783–25810. [[CrossRef](#)]
2. Rodat, S.; Abanades, S.; Boujjat, H.; Chuayboon, S. On the Path toward day and night continuous solar high temperature thermochemical processes: A review. *Renew. Sustain. Energy Rev.* **2020**, *132*, 110061. [[CrossRef](#)]
3. Boujjat, H.; Rodat, S.; Chuayboon, S.; Abanades, S. Experimental and CFD investigation of inert bed materials effects in a high-temperature conical cavity-type reactor for continuous solar-driven steam gasification of biomass. *Chem. Eng. Sci.* **2020**, *228*, 115970. [[CrossRef](#)]
4. Chuayboon, S.; Abanades, S. Thermodynamic and experimental investigation of solar-driven biomass pyro-gasification using H₂O, CO₂, or ZnO oxidants for clean syngas and metallurgical Zn production. *Processes* **2021**, *9*, 687. [[CrossRef](#)]
5. Boujjat, H.; Rodat, S.; Chuayboon, S.; Abanades, S. Experimental and numerical study of a directly irradiated hybrid solar/combustion spouted bed reactor for continuous steam gasification of biomass. *Energy* **2019**, *189*, 116118. [[CrossRef](#)]
6. Boujjat, H.; Rodat, S.; Chuayboon, S.; Abanades, S. Numerical simulation of reactive gas-particle flow in a solar jet spouted bed reactor for continuous biomass gasification. *Int. J. Heat Mass Transf.* **2019**, *144*, 118572. [[CrossRef](#)]
7. Osinga, T.; Olalde, G.; Steinfeld, A. Solar carbothermal reduction of ZnO: Shrinking packed-bed reactor modeling and experimental validation. *Ind. Eng. Chem. Res.* **2004**, *43*, 7981–7988. [[CrossRef](#)]

8. Chuayboon, S.; Abanades, S.; Rodat, S. Solar chemical looping reforming of methane combined with isothermal H₂O/CO₂ splitting using ceria oxygen carrier for syngas production. *J. Energy Chem.* **2020**, *41*, 60–72. [[CrossRef](#)]
9. Villafán-Vidales, H.I.; Abanades, S.; Montiel-González, M.; Romero-Paredes-Rubio, H. Carbo- and methanothermal reduction of tungsten trioxide into metallic tungsten for thermochemical production of solar fuels. *Energy Technol.* **2017**, *5*, 692–702. [[CrossRef](#)]
10. Gokon, N.; Mataga, T.; Kondo, N.; Kodama, T. Thermochemical two-step water splitting by internally circulating fluidized bed of NiFe₂O₄ particles: Successive reaction of thermal-reduction and water-decomposition steps. *Int. J. Hydrog. Energy* **2011**, *36*, 4757–4767. [[CrossRef](#)]
11. Nair, M.M.; Abanades, S. Tailoring hybrid nonstoichiometric ceria redox cycle for combined solar methane reforming and thermochemical conversion of H₂O/CO₂. *Energy Fuels* **2016**, *30*, 6050–6058. [[CrossRef](#)]
12. Chuayboon, S.; Abanades, S.; Rodat, S. Stepwise solar methane reforming and water-splitting via lattice oxygen transfer in iron and cerium oxides. *Energy Technol.* **2020**, *8*, 1900415. [[CrossRef](#)]
13. Nair, M.M.; Abanades, S. Experimental screening of perovskite oxides as efficient redox materials for solar thermochemical CO₂ conversion. *Sustain. Energy Fuels* **2018**, *2*, 843–854. [[CrossRef](#)]
14. Haeussler, A.; Abanades, S.; Jouannaux, J.; Julbe, A. Non-stoichiometric redox active perovskite materials for solar thermochemical fuel production: A review. *Catalysts* **2018**, *8*, 611. [[CrossRef](#)]
15. Chuayboon, S.; Abanades, S.; Rodat, S. High-purity and clean syngas and hydrogen production from two-step CH₄ reforming and H₂O splitting through isothermal ceria redox cycle using concentrated sunlight. *Front. Energy Res.* **2020**, *8*, 128. [[CrossRef](#)]
16. Charvin, P.; Abanades, S.; Beche, E.; Lemont, F.; Flamant, G. Hydrogen production from mixed cerium oxides via three-step water-splitting cycles. *Solid State Ion.* **2009**, *180*, 1003–1010. [[CrossRef](#)]
17. Haeussler, A.; Abanades, S.; Jouannaux, J.; Drobek, M.; Ayril, A.; Julbe, A. Recent progress on ceria doping and shaping strategies for solar thermochemical water and CO₂ splitting cycles. *AIMS Mater. Sci.* **2019**, *6*, 657–684. [[CrossRef](#)]
18. Haeussler, A.; Abanades, S.; Julbe, A.; Jouannaux, J.; Cartoixa, B. Two-step CO₂ and H₂O splitting using perovskite-coated ceria foam for enhanced green fuel production in a porous volumetric solar reactor. *J. CO₂ Util.* **2020**, *41*, 101257. [[CrossRef](#)]
19. Chuayboon, S.; Abanades, S.; Rodat, S. Syngas production via solar-driven chemical looping methane reforming from redox cycling of ceria porous foam in a volumetric solar reactor. *Chem. Eng. J.* **2019**, *356*, 756–770. [[CrossRef](#)]
20. Warren, K.J.; Reim, J.; Randhir, K.; Greek, B.; Carrillo, R.; Hahn, D.W.; Scheffe, J.R. Theoretical and experimental investigation of solar methane reforming through the nonstoichiometric ceria redox cycle. *Energy Technol.* **2017**, *5*, 2138–2149. [[CrossRef](#)]
21. Levêque, G.; Abanades, S. Investigation of thermal and carbothermal reduction of volatile oxides (ZnO, SnO₂, GeO₂, and MgO) via solar-driven vacuum thermogravimetry for thermochemical production of solar fuels. *Thermochimica Acta* **2015**, *605*, 86–94. [[CrossRef](#)]
22. Chuayboon, S.; Abanades, S. Solar-driven chemical looping methane reforming using ZnO oxygen carrier for syngas and Zn production in a cavity-type solar reactor. *Catalysts* **2020**, *10*, 1356. [[CrossRef](#)]
23. Chubukov, B.A.; Rowe, S.C.; Palumbo, A.W.; Wallace, M.A.; Weimer, A.W. Investigation of continuous carbothermal reduction of magnesia by magnesium vapor condensation onto a moving bed of solid particles. *Powder Technol.* **2019**, *365*, 2–11. [[CrossRef](#)]
24. Levêque, G.; Abanades, S.; Jumas, J.-C.; Olivier-Fourcade, J. Characterization of two-step tin-based redox system for thermochemical fuel production from solar-driven CO₂ and H₂O splitting cycle. *Ind. Eng. Chem. Res.* **2014**, *53*, 5668–5677. [[CrossRef](#)]
25. Chambon, M.; Abanades, S.; Flamant, G. Solar Thermal reduction of ZnO and SnO₂: Characterization of the recombination reaction with O₂. *Chem. Eng. Sci.* **2010**, *65*, 3671–3680. [[CrossRef](#)]
26. Levêque, G.; Abanades, S. Thermodynamic and kinetic study of the carbothermal reduction of SnO₂ for solar thermochemical fuel generation. *Energy Fuels* **2014**, *28*, 1396–1405. [[CrossRef](#)]
27. Chuayboon, S.; Abanades, S. Solar metallurgy for sustainable Zn and Mg production in a vacuum reactor using concentrated sunlight. *Sustainability* **2020**, *12*, 6709. [[CrossRef](#)]
28. Perkins, C.; Lichty, P.R.; Weimer, A.W. Thermal ZnO dissociation in a rapid aerosol reactor as part of a solar hydrogen production cycle. *Int. J. Hydrog. Energy* **2008**, *33*, 499–510. [[CrossRef](#)]
29. Chuayboon, S.; Abanades, S. Clean magnesium production using concentrated solar heat in a high-temperature cavity-type thermochemical reactor. *J. Clean. Prod.* **2019**, *232*, 784–795. [[CrossRef](#)]
30. Chuayboon, S.; Abanades, S. Combined ZnO Reduction and methane reforming for co-production of pure zn and syngas in a prototype solar thermochemical reactor. *Fuel Process. Technol.* **2021**, *211*, 106572. [[CrossRef](#)]
31. Abanades, S.; Flamant, G. Hydrogen production from solar thermal dissociation of methane in a high-temperature fluid-wall chemical reactor. *Chem. Eng. Process. Process Intensif.* **2008**, *47*, 490–498. [[CrossRef](#)]
32. Chuayboon, S.; Abanades, S. Thermochemical performance assessment of solar continuous methane-driven ZnO reduction for co-production of pure zinc and hydrogen-rich syngas. *Chem. Eng. J.* **2021**, *429*, 132356. [[CrossRef](#)]
33. Alam, M.E.; Han, S.; Nguyen, Q.B.; Salem Hamouda, A.M.; Gupta, M. Development of new magnesium based alloys and their nanocomposites. *J. Alloy. Compd.* **2011**, *509*, 8522–8529. [[CrossRef](#)]
34. Abanades, S. Metal oxides applied to thermochemical water-splitting for hydrogen production using concentrated solar energy. *ChemEngineering* **2019**, *3*, 63. [[CrossRef](#)]
35. Abanades, S. Thermogravimetry analysis of CO₂ and H₂O reduction from solar nanosized Zn powder for thermochemical fuel production. *Ind. Eng. Chem. Res.* **2012**, *51*, 741–750. [[CrossRef](#)]

36. Abu-Hamed, T.; Karni, J.; Epstein, M. The use of boron for thermochemical storage and distribution of solar energy. *Solar Energy* **2007**, *81*, 93–101. [[CrossRef](#)]
37. Schwab, B.; Ruh, A.; Manthey, J.; Drosik, M. Zinc. In *Ullmann's Encyclopedia of Industrial Chemistry*; Wiley: Hoboken, NJ, USA, 2015.
38. Villasmil, W.; Brkic, M.; Wuillemin, D.; Meier, A.; Steinfeld, A. Pilot scale demonstration of a 100-KWth solar thermochemical plant for the thermal dissociation of ZnO. *J. Solar Energy Eng.* **2013**, *136*, 11011–11016. [[CrossRef](#)]
39. Halmann, M.; Frei, A.; Steinfeld, A. Vacuum carbothermic reduction of Al₂O₃, BeO, MgO-CaO, TiO₂, ZrO₂, HfO₂ + ZrO₂, SiO₂, SiO₂ + Fe₂O₃, and GeO₂ to the metals. A thermodynamic study. *Mineral Process. Extr. Metall. Rev.* **2011**, *32*, 247–266. [[CrossRef](#)]
40. Tian, Y.; Xu, B.; Yang, C.; Yang, B.; Qu, T.; Liu, H.; Dai, Y.; Liu, D. Analysis of magnesia carbothermic reduction process in vacuum. *Metall. Mater. Trans. B* **2014**, *45*, 1936–1941. [[CrossRef](#)]
41. Xie, W.; Chen, J.; Wang, H.; Zhang, X.; Peng, X.; Yang, Y. Kinetics of magnesium preparation by vacuum-assisted carbothermic reduction method. *Rare Metals* **2016**, *35*, 192–197. [[CrossRef](#)]
42. Yang, C.; Tian, Y.; Qu, T.; Yang, B.; Xu, B.; Dai, Y. Analysis of the behavior of magnesium and CO vapor in the carbothermic reduction of magnesia in a vacuum. *J. Magnes. Alloy.* **2014**, *2*, 50–58. [[CrossRef](#)]
43. Xiong, N.; Tian, Y.; Yang, B.; Xu, B.-Q.; Liu, D.-C.; Dai, Y.-N. Volatilization and condensation behaviours of mg under vacuum. *Vacuum* **2018**, *156*, 463–468. [[CrossRef](#)]
44. Chubukov, B.A.; Palumbo, A.W.; Rowe, S.C.; Hirschler, I.; Groehn, A.J.; Weimer, A.W. Pressure dependent kinetics of magnesium oxide carbothermal reduction. *Thermochim. Acta* **2016**, *636*, 23–32. [[CrossRef](#)]
45. Chubukov, B.A.; Palumbo, A.W.; Rowe, S.C.; Wallace, M.A.; Weimer, A.W. Enhancing the rate of magnesium oxide carbothermal reduction by catalysis, milling, and vacuum operation. *Ind. Eng. Chem. Res.* **2017**, *56*, 13602–13609. [[CrossRef](#)]
46. Brkic, M.; Koepf, E.; Meier, A. Solar carbothermal reduction of aerosolized ZnO particles under vacuum: Modeling, experimentation, and characterization of a drop-tube reactor. *Chem. Eng. J.* **2017**, *313*, 435–449. [[CrossRef](#)]